CHEMISTRY

Guest-induced amorphous-to-crystalline transformation enables sorting of haloalkane isomers with near-perfect selectivity

Jia-Rui Wu[1,2], Gengxin Wu[1], Dongxia Li[1], Dihua Dai[1], Ying-Wei Yang[1]*

The separation of haloalkane isomers with distillation-free strategies is one of the most challenging research topics in fundamental research and also gave high guiding values to practical industrial applications. Here, this contribution provides a previously unidentified solid supramolecular adsorption material based on a leggero pillararene derivative BrP[5]L, which can separate 1-/2-bromoalkane isomers with near-ideal selectivity. Activated solids of BrP[5]L with interesting amorphous and nonporous features could adsorb 1-bromopropane and 1-bromobutane from the corresponding equal volume mixtures of 1-/2-positional isomers with purities of 98.1 and 99.0%, respectively. Single-crystal structures incorporating theoretical calculation reveal that the high selectivity originates from the higher thermostability of 1-bromoalkane–loaded structures compared to its corresponding isomer-loaded structures, which could be further attributed to the perfect size/shape match between BrP[5]L and 1-bromoalkanes. Moreover, control experiments using its counterpart macrocycle of traditional pillararene demonstrate that BrP[5]L has better adsorptive selectivity, benefiting from the intrinsic free-rotation phenylene subunit on its backbone.

INTRODUCTION

With the increasing global demand for petrochemicals, the exploitation of new materials or strategies, expected to reduce the environmental impact and operation cost/complexity of industrial separation and purification, is of great significance and imperative. Among these, the energy-efficient separation of haloalkane compounds is a major industrial sustainability challenge (*1*–*3*). The use of macromolecular porous materials, such as metal-organic frameworks (*4*–*6*), zeolites (*7*–*9*), porous organic polymers (*10*–*13*), and covalent organic frameworks (*14*–*18*), in which the building blocks are linked together by covalent or coordinative bonds is considered one solution to solving this problem. Besides, molecular-level porous/nonporous materials, such as hydrogen-bonded organic frameworks (*19*–*21*), supramolecular organic frameworks (*22*–*24*), porous organic cages (*25*–*27*), and nonporous adaptive crystals (*28*–*31*), which are constructed by weak intermolecular interactions, also show promising applications in physical adsorption and energy-efficient separation processes. To date, these macromolecular- or molecular-level adsorption materials have been intensively investigated, and similar features could be summed up as "porosity and crystallinity of its initial state," which means that their adsorption performance is closely correlated with their well-ordered porous frameworks or molecular arrangement.

Supramolecular macrocycle-based crystalline molecular adsorbents have attracted much attention from chemists over the past few years and acquired inestimable benefits from the development of novel synthetic macrocyclic host compounds with distinctive topologies and intriguing properties (*32*–*36*). With the increased understanding of host-guest chemistry, structure-function relationship, noncovalent interactions, and dynamic molecular assembly, the creative design of macrocycle-based supramolecular materials with growing complexity, functionality, and applicability could be implemented with great ease.

Pillararenes, a new generation of supramolecular hosts, have been classified as one of the most iconic macrocyclic containers among the well-established ones (e.g., crown ethers, cyclodextrins, cucurbiturils, and calixarenes) (*37*–*39*) and gained tremendous momentum during the modern supramolecular chemistry boom. Recently, we have presented an example of pillar[5]arene-derived macrocyclic receptor, named permethylated leggero pillar[5]arene (**MeP[5]L**) (*40*), in which two methoxy functionalities on a single one of the subunits of traditional permethylated pillar[5]arene were selectively removed. We also found that the amorphous powder of **MeP[5]L** can physically adsorb certain types of guest vapors accompanied by the molecular packing transition from the initially chaotic state to various ordered states. Inspired by this, we speculate that the macrocycle-based molecular materials constructed from disordered molecular building blocks without any porosity and crystallinity could also be excellent potentially applied in molecular separation.

In this work, we report the whole family of leggero pillar[*n*]arenes (P[*n*]Ls for short) and use the amorphous nonporous powders of perbromoethylated leggero pillar[5]arene (**BrP[5]L**) to achieve a super-efficient adsorptive separation of 1-/2-bromoalkane isomers (Fig. 1, A and B). We find that **BrP[5]L** can separate 1-bromopropane (**1-BPR**) from **2-BPR** with 98.1% purity (Fig. 1C) and separate 1-bromobutane (**1-BBU**) from **2-BBU** with 99.0% purity (50:50, v/v) (Fig. 1D), which is superior to the counterpart in traditional pillararenes, perbromoethylated pillar[5]arene (**BrP[5]A**). The precisely sorting capability can be ascribed to the superior cavity adaptability and tunability, benefiting from its inherent free-rotation phenylene subunit. Powder x-ray diffraction (PXRD) reveals that this adsorptive separation process is also a bottom-up molecular assembly approach from the initial guest-free amorphous to the last guest-loaded crystalline structures driven by weak intermolecular interactions in the solid state. Moreover, removing

[1]International Joint Research Laboratory of Nano-Micro Architecture Chemistry, College of Chemistry, Jilin University, 2699 Qianjin Street, Changchun 130012, P. R. China. [2]Key Laboratory of Automobile Materials of Ministry of Education and School of Materials Science and Engineering, Jilin University, 5988 Renmin Street, Changchun 130025, P. R. China.
*Corresponding author. Email: ywyang@jlu.edu.cn, yyang@chem.ucla.edu

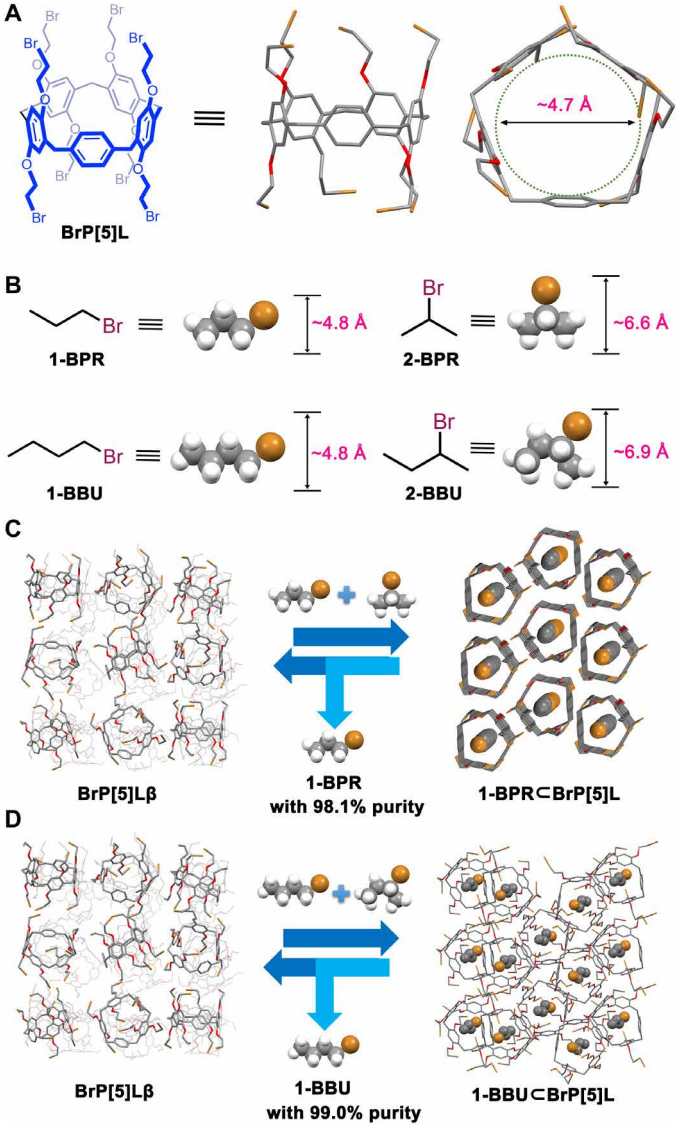

Fig. 1. A general strategy for separating 1-/2-bromoalkane isomers via guest-induced restructuring of amorphous macrocyclic hosts. Chemical structures of (**A**) perbromoethylated leggero pillar[5]arene (**BrP[5]L**) and (**B**) 1-bromopropane (**1-BPR**), **2-BPR**, 1-bromobutane (**1-BBU**), and **2-BBU**. The size of the cavity in **BrP[5]L** was calculated to be 4.7 Å. The effective sizes of **1-BPR**, **1-BBU**, **2-BPR**, and **2-BBU** were calculated as 4.8, 4.8, 6.6, and 6.9 Å, respectively. Schematic representation of the separation process and mechanism of (**C**) **1-BPR** from **1-BPR/2-BPR** isomer mixture and (**D**) **1-BBU** from **1-BBU/2-BBU** isomer mixture using **BrP[5]Lβ**.

1-bromoalkanes from 1-bromoalkanes–loaded **BrP[5]L** structures leads to the original guest-free amorphous state, making **BrP[5]L** highly recyclable without losing any performance.

RESULTS

Synthesis and characterization of P[*n*]Ls

Selective removal of two hydroxy or alkoxy groups on one subunit of traditional P[*n*]As turns out to be much more unachievable because of the extreme difficulty to precisely crack two aryl-O bonds on one alkoxybenzene subunit. Previously, we discovered that the critical step for **MeP[5]L** synthesis is the initial construction of two kinds of coupling precursors (*40*). Accordingly, in this research, we successfully synthesized per-hydroxylated P[5]L (**P[5]L**), perethylated P[5]L (**EtP[5]L**), perethylated P[6]L (**EtP[6]L**), **BrP[5]L**, and two other important functional derivatives P[5]L-1 and P[5]L-2. Specifically, macrocyclization of **EtP[5]L** and **EtP[6]L** could be implemented by fragment coupling of two kinds of easily synthesized precursors (1 and 2 or 1 and 3) with paraformaldehyde in $CHCl_2$ or $CHCl_3$ in the presence of a catalytic amount of Lewis acid $BF_3{\cdot}O(Et)_2$ at room temperature (Fig. 2A and figs. S1 to S4), resulting in **EtP[5]L** and **EtP[6]L** in isolated yields of 19 and 9%, respectively (see the Supplementary Materials). Whereafter, **P[5]L** could be qualitatively obtained by the O-dealkylation of **EtP[5]L** with an excess amount of BBr_3 (fig. S5), indisputably confirming the postmodification capability of P[*n*]Ls.

The synthesis of **BrP[5]L**, bearing eight bromoethyl moieties, was accomplished by a facile three-step synthetic approach from P[5]L (Fig. 2A and fig. S6). First, macrocyclic intermediate P[5]L-1, i.e., ethoxycarbonyl-substituted P[5]L, can be prepared in a yield of 47% by reacting **P[5]L** with excess ethyl bromoacetate via a nucleophilic substitution reaction. Whereafter, the reduction of P[5]L-1 with $LiAlH_4$ afforded the octanol P[5]L-2 in 45% yield, followed by further bromination by CBr_4 and PPh_3 to give the target compound **BrP[5]L** in 50% yield. The whole synthetic approach of these derivatives is highly convenient, efficient, and smooth, indicating the versatility and universality of P[*n*]L macrocycles.

P[5]L, **EtP[5]L**, **EtP[6]L**, and **BrP[5]L** were fully characterized by $^1H/^{13}C$ nuclear magnetic resonance (NMR) spectroscopies, matrix-assisted laser desorption/ionization–time-of-flight mass spectrometry (MALDI-TOF MS) spectroscopy, and density functional theory (DFT) analysis (Fig. 2B and figs. S7 to S30). The guest-binding capability, derived from the strengths and weaknesses of intermolecular interactions, more or less relies on the in-cavity electrical properties in supramolecular macrocyclic receptors. Similar to traditional pillararenes, the electrostatic potential maps of P[*n*]Ls also exhibit π-electron–rich aromatic cavities with negative potential, confirming that the selective removal of functionalities on a single one phenylene subunit of traditional pillararenes has no noticeable impact on its in-cavity binding performance in the viewpoint of electrical characters. All energy-minimized structures of **P[5]L**, **EtP[5]L**, **EtP[6]L**, and **BrP5L** render a noncylindrical C_i molecular conformation with the unsubstituted phenylene subunit tilt to the inner cavity in varying degrees (Fig. 2B), which is in sharp contrast to the traditional pillar-shaped pillar[5]arenes with D_{5h} symmetry.

Although one unsubstituted phenylene exists among the ring-forming subunits, P[*n*]Ls still show large enough and effective cavities for binding with different species in the solid-state (super) structure. As in Fig. 3 and figs. S31 to S36, by the stabilization of multiple intermolecular interactions, **P[5]L**, **MeP[5]L**, **EtP[5]L**, and **BrP[5]L** can encapsulate acetone, *n*-hexane (*n*-Hex), dichloromethane (DCM), or CH_3CN molecule in the cavity or lattice voids to form acetone⊂**P[5]L**, *n*-Hex⊂**MeP[5]L**, DCM⊂**MeP[5]L**, CH_3CN⊂**MeP[5]L**, CH_3CN⊂**EtP[5]L**, and $2(CH_3CN)$⊂**BrP[5]L**, respectively. Furthermore, the structural flexibility and adaptability of P[5]Ls were proven unambiguously by x-ray crystallography. Concretely, **MeP[5]L** in *n*-Hex⊂**MeP[5]L** adopts an almost pillar-shaped structure, and the unsubstituted phenylene subunit has a dihedral angle (DA) of 89.9° with the pentagonal plane formed by its five methylene carbon atoms (Fig. 3B). **MeP[5]L** exhibited a distinct conformational

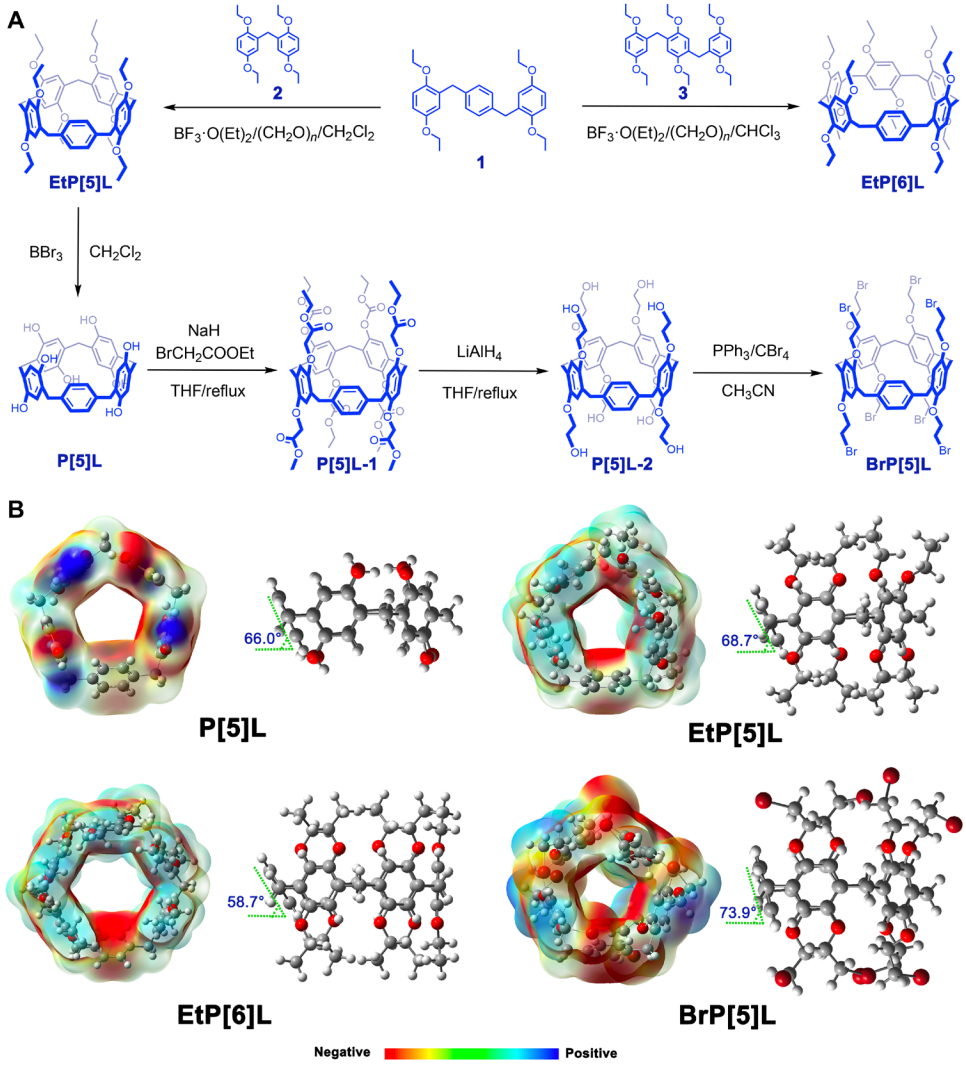

Fig. 2. Synthesis and structures. (**A**) Synthetic route to P[*n*]Ls, that is, **P[5]L**, **EtP[5]L**, **EtP[6]L**, and functional P[5]L derivatives P[5]L-1, P[5]L-2, and **BrP[5]L**. (**B**) Energy-minimized structures and electrostatic potential surfaces of **P[5]L**, **EtP[5]L**, **EtP[6]L**, and **BrP[5]L** showing the π-electron–rich character of the aromatic cavity and the noncylindrical molecular conformation of the P[5]Ls scaffold.

change in DCM⊂**MeP[5]L** and CH_3CN⊂**MeP[5]L**, where the relative DA values are 58.0° and 61.2° (Fig. 3, C and D), respectively, rendering an approximate 30° angle change in comparison with **MeP[5]L** in *n*-Hex⊂**MeP[5]L**. Besides, the relative DA values of **EtP[6]L** and **BrP5L** in CH_3CN⊂**EtP[5]L** and 2(CH_3CN)⊂**BrP[5]L** are 75.3° and 50.9° (Fig. 3, E and F), respectively, displaying obvious distinctions between each other and also varying from **MeP[5]L** in CH_3CN⊂**MeP[5]L** as aforementioned, which suggest that the conformational diversity of P[5]Ls was affected by not only the guest species but also the substituent groups. All the above results reflect the remarkable adaptability and tunability of the binding cavity in P[5]L macrocycles, benefiting from the free-rotation phenylene subunit.

Preparation and characterization of activated BrP[5]L

For adsorptive separation, guest-free– and thermodynamically favored crystalline structure of **BrP[5]L** (**BrP[5]Lα**) was obtained from recrystallization in the mixture of 2-bromobutane and methylcyclohexane (fig. S37). The resulting crystals were then subjected to vacuum at elevated temperature (110°C) for 6 hours to obtain activated adsorptive separation materials. Thermogravimetric analysis (TGA) proved that the activated powder was fully desolvated (figs. S38 and S39). PXRD demonstrated that the solids transformed from crystalline **BrP[5]Lα** to amorphous state (**BrP[5]Lβ**) upon heating (Fig. 4A and fig. S40), which could be ascribed to the relatively low melting point (138°C) of **BrP[5]L**, as proved by differential scanning calorimetry (DSC) experiment (fig. S41). The Brunauer-Emmett-Teller surface area of **BrP[5]Lβ** was determined to be 3.83 m^2/g by the 77-K N_2 sorption test (fig. S42), indicating its nonporous feature.

Single-component bromoalkane isomer adsorption experiments

Despite its nonporous nature, the adsorption property of **BrP[5]Lβ** toward 1-bromoalkane and 2-bromoalkane was first investigated through time-dependent single-component solid-vapor sorption

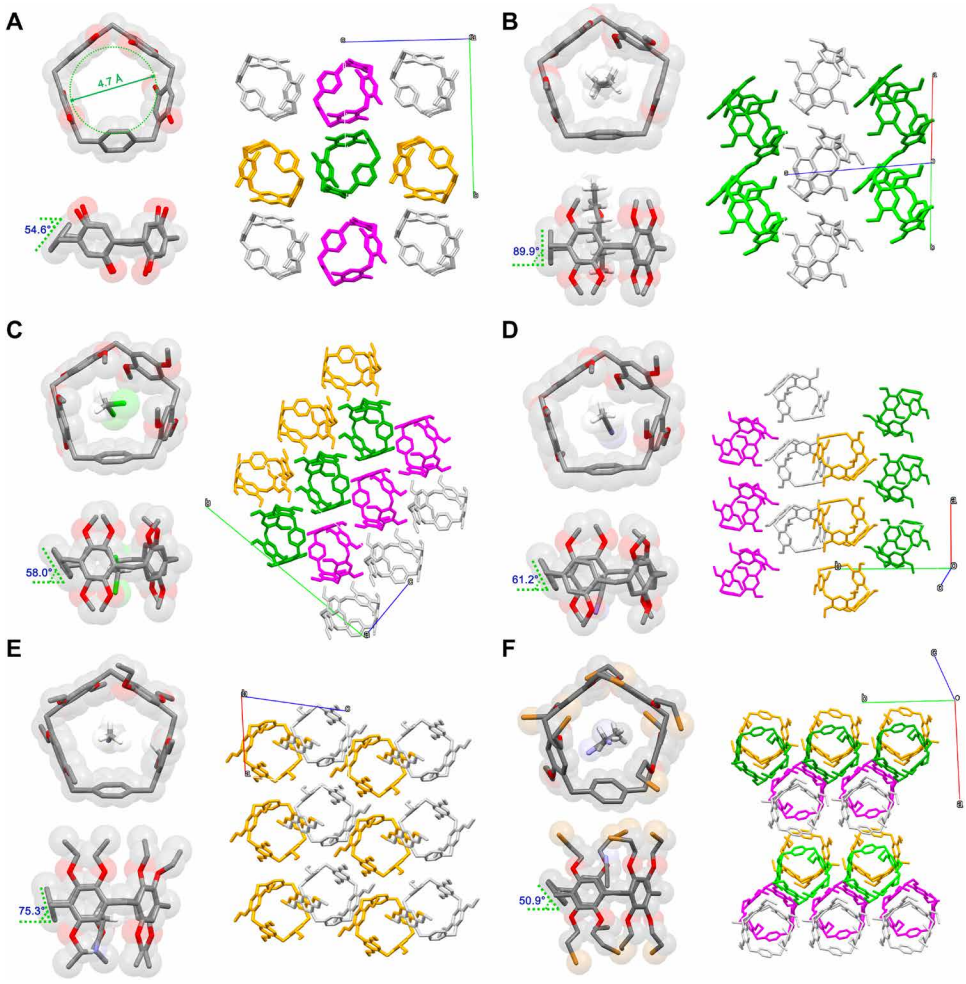

Fig. 3. Solid-state (super)structure of P[5]Ls. X-ray single-crystal structures of (**A**) **P[5]L**, (**B**) *n*-Hex⊂**MeP[5]L**, (**C**) DCM⊂**MeP[5]L**, (**D**) CH_3CN⊂**MeP[5]L**, (**E**) CH_3CN⊂**EtP[5]L**, and (**F**) 2(CH_3CN)⊂**BrP[5]L** showing the structural adaptability and tunability of the binding cavity in P[5]Ls macrocycles that are benefiting from the free-rotation phenylene subunit.

experiments. As shown in Fig. 4 (B and C), **1-BPR**, **2-BPR**, **1-BBU**, and **2-BBU** can all be adsorbed by **BrP[5]Lβ**, and the adsorption rates of **1-BPR** and **2-BPR** were slightly faster than **1-BBU** and **2-BBU**, which took only about 1 to 2 hours to reach the saturation points upon adsorption. ^{1}H NMR spectra and TGA results further verified the adsorption and storage capability of **BrP[5]Lβ**. The uptake amounts of **1-BPR**, **2-BPR**, **1-BBU**, and **2-BBU** can be calculated as ca. 1.0, 2.0, 1.0, and 1.5 mol/mol **BrP[5]L** at equilibrium, respectively (figs. S43 to S50).

PXRD experiments were implemented to study the structural changes of **BrP[5]Lβ** upon uptake of bromoalkane vapors. As shown in Fig. 4 (D and E), **BrP[5]Lβ** in amorphous state exhibited sharp peaks after adsorption of **1-BPR**, **2-BPR**, **1-BBU**, and **2-BBU**, which indicated that these guest-free disordered hosts transformed into new guest-loaded structures and gained crystallinity to some extent via guest-induced intermolecular interactions. Moreover, the **BrP[5]L** patterns after adsorption of **1-BPR** or **2-BPR** were different from each other, suggesting the formation of two new **BrP[5]L** structures. Similar results were also observed after uptake of **1-BBU** and **2-BBU**.

Structural analysis of BrP[5]L with bromoalkane isomers

To reveal these new guest-containing structures, we obtained single crystals of **BrP[5]L** loaded with **1-BPR**, **1-BBU**, and **2-BPR** (Fig. 5). By the stabilization of multiple C—H···π (interact site distances of 2.521, 2.648, 2.775, and 3.004 Å), C—H···O (3.330 and 3.348 Å), and C—H···Br (3.394 Å) interactions (fig. S51), **BrP[5]L** can encapsulate one **1-BPR** to form **1-BPR**⊂**BrP[5]L** complex (space group *C*2, monoclinic) in the crystalline state. The pentagonal **BrP[5]L** molecules assemble in a herringbone packing mode. Thus, no atomic-scale channel could be found in the structure because of the two adjacent **BrP[5]L** molecules being staggered from each other (Fig. 5A). Moreover, the PXRD pattern of **BrP[5]L** after uptake of **1-BPR** matched well with the simulated pattern (fig. S52), suggesting that the adsorption of **1-BPR** led to the structural transition from disordered **BrP[5]Lβ** to **1-BPR**⊂**BrP[5]L**. As for **1-BBU**–loaded **BrP[5]L** structure (**1-BBU**⊂**BrP[5]L**), **BrP[5]L** molecules were crystallized in the space group *P*-1 (triclinic), and a 1:1 host-guest complex stabilized by C—H···π (interact site distances of 2.761, 2.838, 2.791, and 3.011 Å), C—H···O (2.979 and 3.374 Å), and C—H···Br (3.348 and 3.379 Å) interactions was also observed (fig. S53). **BrP[5]L** forms

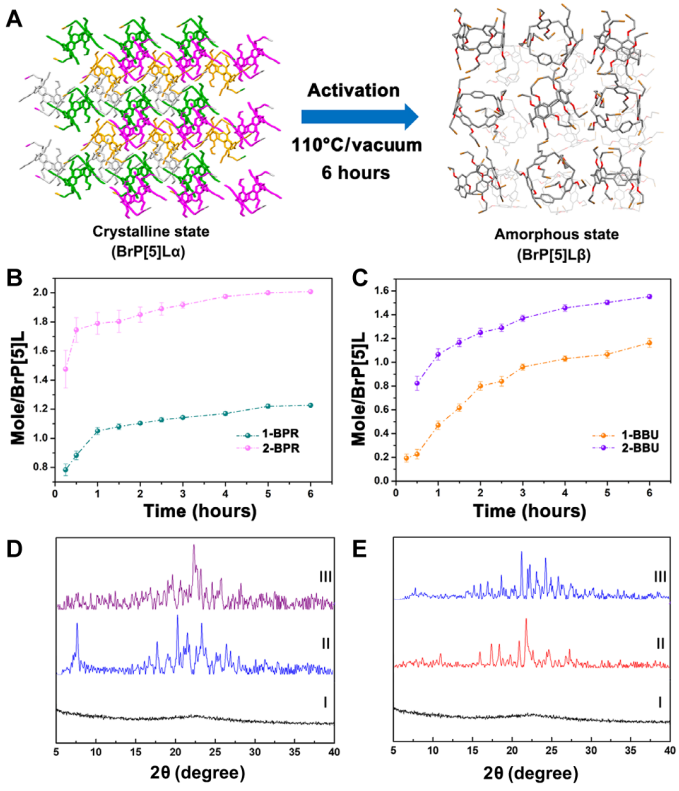

Fig. 4. Single-component bromoalkane isomer adsorption experiments. (**A**) Schematic representation of the phase transition from the initial guest-free crystalline state (**BrP[5]Lα**) to the guest-free amorphous state (**BrP[5]Lβ**) upon heating. (**B** and **C**) Time-dependent **BrP[5]Lβ** solid-vapor sorption plots for single-component (B) bromopropane isomer vapor and (C) bromobutane isomer vapor. (**D**) PXRD patterns of **BrP[5]L**: (I) original **BrP[5]Lβ**, after adsorption of (II) **2-BPR** vapor, and (III) **1-BPR** vapor. (**E**) PXRD patterns of **BrP[5]L**: (I) original **BrP[5]Lβ**, after adsorption of (II) **2-BBU** vapor, and (III) **1-BBU** vapor.

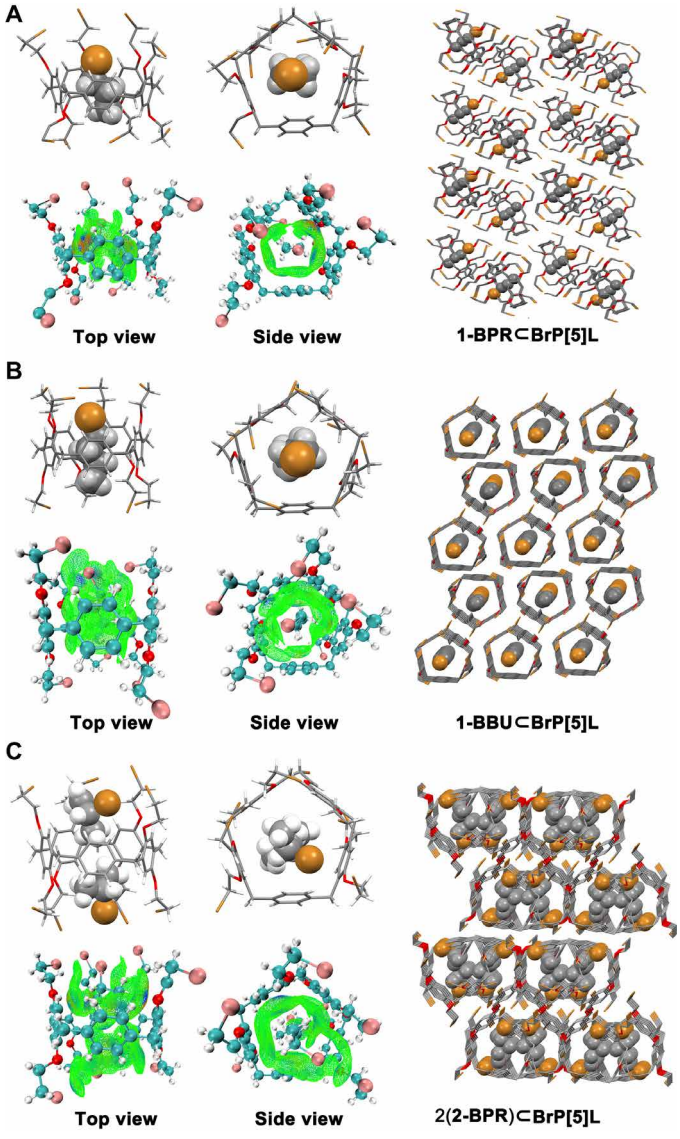

Fig. 5. Structural analysis of BrP[5]L with bromoalkane isomers. Solid-state superstructures and intermolecular binding isosurfaces (visual study of weak intermolecular interaction) of (**A**) **1-BPR⊂BrP[5]L**, (**B**) **1-BBU⊂BrP[5]L**, and (**C**) **2-BPR⊂BrP[5]L**.

regularly window-to-window packing mode, resulting in infinite honeycomb-like one-dimensional (1D) channels with **1-BBU** threaded through (Fig. 5B). Note that there are still a small quantity of disordered **1-BBU** molecules located outside the cavity and links neighboring **BrP[5]L** through weak van der Waals contacts in **1-BBU⊂BrP[5]L** (fig. S54). Despite many attempts, the PXRD pattern of **BrP[5]L** after taking up **1-BBU** gave a poor quality of match with the corresponding simulated pattern from **1-BBU⊂BrP[5]L** (fig. S55), presumably due to the lack of disordered **1-BBU** molecules in the lattice voids as the crystal structure presented to us. Subsequently, DSC experiments were carried out to study the desorption behaviors of **1-BPR⊂BrP[5]L** and **1-BBU⊂BrP[5]L**. Contrary to the relatively normal boiling points of **1-BPR** and **1-BBU** (boiling point of **1-BPR**: 71°C and boiling point of **1-BBU**: 101°C), **1-BPR⊂BrP[5]L** and **1-BBU⊂BrP[5]L** began to release **1-BPR** and **1-BBU** molecules at ca. 125° and 105°C (figs. S56 and S57), which indicated that the thermostability of herringbone packing mode without specific channels in **1-BPR⊂BrP[5]L** is higher than the honeycomb-like packing mode in **1-BBU⊂BrP[5]L**, and more heat is needed to desorb the guest species.

In terms of 2-bromoalkane–loaded structures, single crystals of **BrP[5]L** loaded with **2-BPR** (**2-BPR⊂BrP[5]L**) were also obtained by slow evaporation of a **2-BPR** solution of **BrP[5]L**. Despite numerous attempts, no suitable crystal structure of **2-BBU**–loaded **BrP[5]L** (**2-BBU⊂BrP[5]L**) was obtained, which could be ascribed to the molecular chirality of **2-BBU** and the size mismatch between **2-BBU** and the cavity of **BrP[5]L**. In **2(2-BPR)⊂BrP[5]L**, **BrP[5]L** hosts were crystallized in the space group *P*-1 (triclinic) and formed a 1:2 host-guest assembly with **2-BPR** (Fig. 5C). Driven by the stabilization of C—H···π (interact site distances of 2.880, 2.835, and 3.190 Å), C—H···O (2.786, 2.928, and 3.076 Å), and C—H···Br (distance of 3.183 Å) interactions, two **2-BPR** molecules irregularly reside in the cavity rims of **BrP[5]L**, and the protruded Br atoms further interact with the neighboring **BrP[5]L** through C—H···Br (distance of 3.031 Å) interaction (fig. S58). Besides, **BrP[5]L** in **2(2-BPR)⊂BrP[5]L** exhibited a 2D layer-like superstructure network with the neighboring layers stacking in a staggered packing mode; thus, no specific channels could be found in the structure (Fig. 5C). The PXRD pattern of **BrP[5]L** after adsorption of **2-BPR**

vapor was consistent with that simulated from **2-BPR⊂BrP[5]L** (fig. S59), confirming that the uptake of **2-BPR** resulted in a phase transition from nonporous **BrP[5]Lβ** to **2-BPR⊂BrP[5]L**.

To prejudge the relative stability of **BrP[5]L** loaded with 1-bromoalkane and 2-bromoalkane, independent gradient model (IGM) analyses (visual study of weak interaction) were carried out (Fig. 5). The intermolecular binding isosurfaces revealed that the host-guest interactions of **1-BPR⊂BrP[5]L** and **1-BBU⊂BrP[5]L** are mainly concentrated in the center of the electron-rich cavity of **BrP[5]L**. Meanwhile, the guest molecules are fully encapsulated. In comparison, the areas of the binding isosurfaces between **2-BPR** and **BrP[5]L** are centered mainly around the rims of the cavity, which binding mode is sustained primarily by the substituent groups of **BrP[5]L**. In addition, DSC experiments were conducted, and a broad endothermic peak ranging from 40° to 120°C was found in both **2-BPR⊂BrP[5]L** and **2-BBU⊂BrP[5]L** (figs. S60 and S61), representing the release of **2-BPR** or **2-BBU** molecules. As compared with the higher desorption temperatures and smaller endothermic ranges of both **1-BPR⊂BrP[5]L** and **1-BBU⊂BrP[5]L** as aforementioned, we can deduce that the in-cavity binding between 1-bromoalkanes and **BrP[5]L** with more suitable host-guest size/shape match will have higher thermostability than their corresponding 2-bromoalkanes–loaded structures.

Mixture vapor adsorption experiments of BrP[5]L

Given the different crystal structures and thermostabilities of **BrP[5]L** upon adsorption, we here investigated whether **BrP[5]Lβ** could separate 1-/2-bromoalkane isomers. First, a time-dependent solid-vapor (from an equimolar **1-BPR/2-BPR** or **1-BBU/2-BBU** mixture) sorption experiment was carried out. As shown in Fig. 6 (B and C), the uptake amounts of **1-BPR** and **1-BBU** increased with time and took about 2 and 5 hours to reach each saturation point, respectively. In sharp contrast to the single-component adsorption plots, the sorption of 2-bromoalkanes was negligible from beginning to end, and **BrP[5]Lβ** maintained its selectivity toward 1-bromoalkanes all along. Consistent with the crystal structures, the adsorption amounts of **1-BPR** and **1-BBU** were determined as nearly one **1-BPR** or **1-BBU/BrP[5]L**, which were also in good agreement with the single-component adsorption experiments as above mentioned (figs. S62 and S63). The PXRD patterns of **BrP[5]Lβ** after adsorption of the 1-/2-bromoalkane isomer mixture vapors matched well with that upon uptake of the single-component 1-bromoalkane vapors (Fig. 6, C and D). Gas chromatography (GC) tests showed that the purities of **1-BPR** and **1-BBU** adsorbed in **BrP[5]Lβ** were determined to be 98.1 and 99.0% (Fig. 6E and figs. S64 and S65), respectively, further supporting the remarkably high selectivity of **BrP[5]Lβ** for 1-bromoalkane isomers. Electrostatic potential maps for the complexes of **1-BPR⊂BrP[5]L** and **1-BBU⊂BrP[5]L** exhibited that electrons in the original electron-deficient **1-BPR** and **1-BBU** fully delocalized in the whole electron-rich cavity of **BrP[5]Lβ** upon adsorption (Fig. 6G), again confirming that the high selectivity not only arose from the stability of the newly formed crystal superstructure after guest adsorption but also came from the strong intermolecular interactions by the perfect size match between **BrP[5]L** and 1-bromoalkane isomers.

In industry, recyclability is one of the vital parameters to evaluate an adsorbent. We proved that **BrP[5]Lβ** with amorphous nature could be wholly regenerated by simply heating **1-BBU⊂BrP[5]L** at 120°C under vacuum, as characterized by ^{1}H NMR, TGA, and PXRD (figs. S66 to S69). Moreover, the newly formed **BrP[5]Lβ** still maintained its selectivity for **1-BBU** vapor from an equal volume mixture of **1-BBU/2-BBU** without any detectable degradation after recycling six times (Fig. 6F).

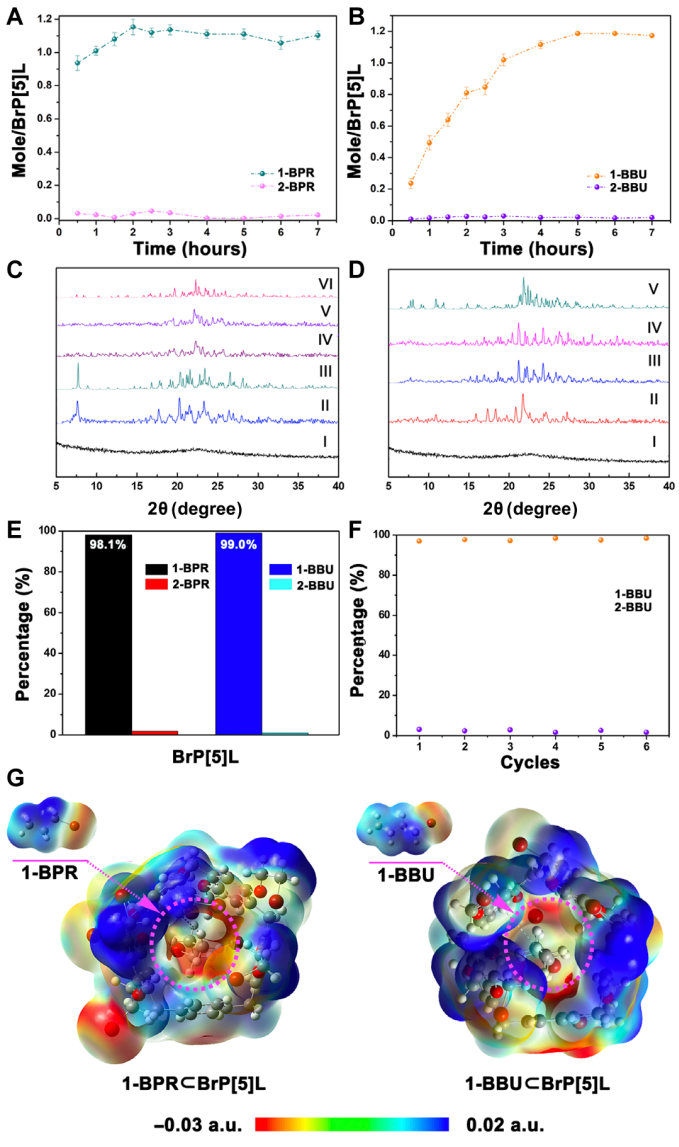

Fig. 6. Mixture vapor adsorption experiments of BrP[5]L. (**A** and **B**) Time-dependent **BrP[5]Lβ** solid-vapor adsorption plots for a 1:1 vapor mixture of (A) bromopropane isomers and (B) bromobutane isomers. (**C**) PXRD patterns of **BrP[5]L**: (I) original **BrP[5]Lβ**; (II) after adsorption of **2-BPR** vapor, (III) simulated from the single-crystal structure of **2-BPR⊂BrP[5]L**, (IV) after adsorption of **1-BPR** vapor, (V) after adsorption of the **1-BPR** and **2-BPR** mixture vapor, and (VI) simulated from the single-crystal structure of **1-BPR⊂BrP[5]L**. (**D**) PXRD patterns of **BrP[5]L**: (I) original **BrP[5]Lβ**, (II) after adsorption of **2-BBU** vapor, (III) after adsorption of **1-BBU** vapor, (IV) after adsorption of the **1-BBU** and **2-BBU** mixture vapor, and (V) simulated from the single-crystal structure of **1-BBU⊂BrP[5]L**. (**E**) Relative amounts of 1- and 2-bromoalkane isomers adsorbed by **BrP[5]Lβ** over 7 hours as measured by GC. (**F**) Relative uptake of **1-BBU** and **2-BBU** by **BrP[5]Lβ** over 7 hours after **BrP[5]L** was recycled six times. (**G**) Electrostatic potential maps of **1-BPR**, **1-BPR⊂BrP[5]L**, **1-BBU**, and **1-BBU⊂BrP[5]L** revealing that electrons in the original electron-rich 1-bromoalkanes delocalized in the whole host-guest complexes because of strong intermolecular interactions. a.u., arbitrary units.

Controlled experiments by comparison with traditional pillararene

Given that **BrP[5]Lβ** exhibited high selectivity to 1-bromoalkane isomers, we were interested in finding some differences in the adsorption performance between **BrP[5]Lβ** and its counterpart macrocyclic arene of **BrP[5]A** (**BrP[5]Aα**) in traditional pillararenes (Fig. 7A). Therefore, controlled adsorption experiments by using **BrP[5]Aα** were carried out. Single-component solid-vapor adsorption experiments confirmed that the uptake amounts of **1-BPR**, **2-BPR**, **1-BBU**, and **2-BBU** could all be calculated as about one molecule per **BrP[5]A** at saturation (figs. S70 to S79), respectively. Consistent with **BrP[5]Lβ**, mixture vapor adsorption experiments revealed that **BrP[5]Aα** also exhibited an outstanding selectivity to 1-bromoalkane isomers (figs. S80 to S85). GC experiments demonstrated that the selectivities of **BrP[5]Aα** for **1-BPR** and **1-BBU** were 96.9 and 96.0%, respectively (Fig. 7B). Although the adsorptive selectivity of **BrP[5]Aα** toward 1-bromoalkane isomers is good, there are still substantial gaps in comparison with **BrP[5]Lβ**. To reveal the mechanism of the selectivity difference between **BrP[5]A** and **BrP[5]L**, we obtained single crystals of **BrP[5]A** loaded with **1-BBU** (**1-BBU⊂BrP[5]A**) via a solution growth method (Fig. 7C). In line with **1-BBU⊂BrP[5]L**, **BrP[5]A** molecules in **1-BBU⊂BrP[5]A** were crystallized in the space group *P*-1 (triclinic) and formed a 1:1 host-guest complex with **1-BBU** by the stabilization of multiple C—H···π (distances of 2.773, 2.689, 2.958, and 3.001 Å), C—H···O (distances of 2.993 and 3.057 Å), and C—H···Br (distances of 3.232 and 3.333 Å) interactions (fig. S86). Intriguingly, we found that **BrP[5]L** in **1-BBU⊂BrP[5]L** exhibited a distinct guest-induced conformational change, where the DA value between the unsubstituted phenylene subunit and the pentagonal plane is 70.6°, in sharp contrast to the pillar-shaped molecular conformation of **BrP[5]A** in **1-BBU⊂BrP[5]A** (fig. S87). Thus, the better adsorptive/guest selectivity than **BrP[5]A** is ascribed to the superior adaptability and tunability of the binding cavity in **BrP[5]L** macrocycle due to the free-rotation phenylene subunit.

In addition, the structural flexibility of **P[5]Ls** was also tested and proved by DFT analysis. Conformational free energies of **P[5]L** were calculated by rotating the DA of the unsubstituted phenylene subunit every 20° concerning the pentagonal plane (Fig. 7D). Taking a point-to-point comparison with the corresponding conformational free energy of traditional pillar[5]arene (**P[5]A**) by rotating one of its phenylene subunits, we can easily find that the rotation of the subunit in **P[5]A** is challenging, where the maximum rotational barrier reaches up to more than 80 kcal/mol, showing a barrier nearly 20-fold larger than that of **P[5]L** (about 4 kcal/mol). Besides, compared with the single low-energy state point at the pillar-shaped molecular conformation of **P[5]A** (90° DA), the energy changes of all points during the rotation in **P[5]L** were minor. These results indicated a markedly increased flexibility of macrocyclic backbone of **P[5]L**, allowing the free-rotation phenylene subunit to adopt a preferred perpendicular or tilted conformation and again confirmed the better tunability of the cavity size, endowing **P[5]Ls** with more potential for high selective guest adsorption as demonstrated by the aforementioned controlled experiments.

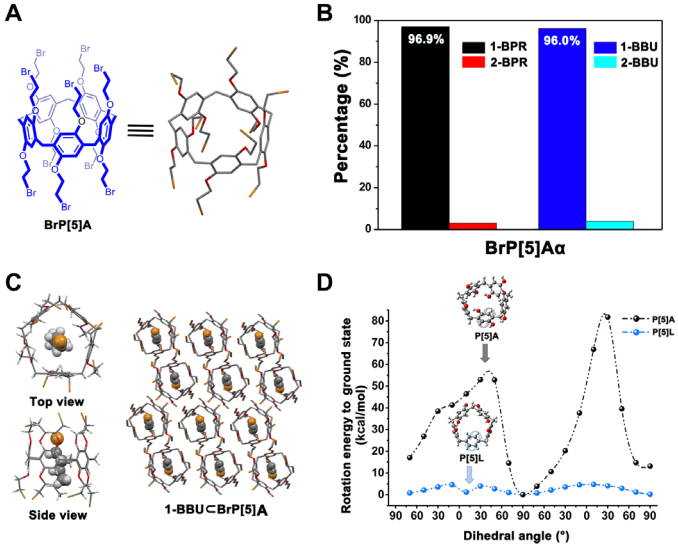

Fig. 7. Controlled experiments by comparison with traditional pillararene. (**A**) Chemical structure of **BrP[5]A**. (**B**) Relative amounts of 1- and 2-bromoalkane isomers adsorbed by **BrP[5]Aα** over 7 hours as measured by GC. (**C**) Single-crystal structure of **1-BBU⊂BrP[5]A**. (**D**) DFT-calculated rotational free energy comparison between the free-rotation phenylene subunit of **P[5]L** and a subunit of **P[5]A**.

DISCUSSION

In conclusion, we have successfully developed a flexible macrocycle-based molecular-level adsorption material, amorphous solids of **BrP[5]L**, which can separate 1-/2-bromoalkane isomers with near-ideal selectivity. In conjunction with theoretical calculation and TG-DSC, single-crystal structures revealed that the adsorption selectivity mostly came from the higher thermostability of 1-bromoalkanes–loaded structures than its corresponding isomers-loaded structures, which could be further attributed to the perfect size/shape match between **BrP[5]L** and 1-bromoalkanes. Controlled experiments using its counterpart macrocyclic arene from traditional pillararenes demonstrated that **BrP[5]Lβ** had better sorting abilities by virtue of its superior structural adaptability and cavity-size tunability arising from the unsubstituted free-rotation phenylene subunit. In addition, the reversible transitions between the guest-free amorphous and the guest-containing crystalline state made **BrP[5]L** highly recyclable. On reflection, the novelty of this work can be summarized as follows: (i) We presented a family of skeleton-trimmed pillararene derivatives, leggero pillar[*n*]arene, and meanwhile, a nearly perfect separation of bromoalkane isomers using macrocycle-based molecular adsorbent is achieved; (ii) we proved that adsorption material without any porosity and crystallinity could also be greatly applied in molecular adsorptive separation; and (iii) new strategies to strengthen the structural adaptability and guest selectivity for traditional pillararenes have been put forward. Ongoing studies in our laboratory focus on constructing more supramolecular-level adsorptive separation materials based on the P[*n*]L family for applications in other demanding separations, such as sorting isotopes and chiral compounds.

MATERIALS AND METHODS

Materials availability

All reagents were purchased from commercial suppliers and used without further purification unless stated otherwise. The synthetic

methods of **P[5]L**, **EtP[5]L**, **EtP[6]L**, **P[5]L-1**, and **BrP[5]L** are described in detail in the Supplementary Materials. **1-BPR**, **2-BPR**, **1-BBU**, and **2-BBU** were purchased from Sigma-Aldrich. Activated amorphous **BrP[5]L**, referred to as **BrP[5]Lβ**, was obtained by heating the thermodynamically favored guest-free crystalline structure of **BrP[5]L**, that is, **BrP[5]Lα**, under reduced pressure at 110°C for 6 hours.

Material characterization

^{1}H and ^{13}C NMR spectra were recorded at 298 K on a Bruker AVANCE III 400-MHz instrument at room temperature. Chemical shifts were referenced to tetramethylsilane. Mass spectra were recorded on Bruker Daltonics Autoflex Speed Series: High-Performance MALDI-TOF Systems and a Bruker Agilent1290 micrOTOF-Q II high-resolution MS instrument. PXRD measurements were collected on a PANalytical B.V. Empyrean powder diffractometer operating at 40 kV/30 mA using the Cu Kα line (λ = 1.5418 Å). Following procedures previously described in (*41*), data were measured over the range 5° to 40° in 5°/min steps over 7 min. Single-crystal XRD data were measured by a Bruker D8 Venture diffractometer using the ω-scan mode with graphite-monochromator Mo Kα radiation (λ = 0.71073 Å) and Ga Kα (λ = 1.34139 Å). The structures were solved with SHELXD (*42*), with SHELXT (*43*), or by the direct methods with SHELXS-2014 (*44*); refined by full-matrix least squares on $|F|^2$ by SHELXL (*45*); and interfaced through the program Olex2 (*46*). TGA was carried out using a simultaneous thermal analyzer 449 F3 analyzer (NETZSCH Instruments) with an automated vertical overhead thermobalance. The samples were heated at 10°C/min using N_2 as the protective gas. DSC analysis was done on a DSC Q20 at a heating rate of 10°C/min at a nitrogen atmosphere. Low-pressure gas adsorption measurements were performed on a Micromeritics Accelerated Surface Area and Porosimetry System 2020 surface area analyzer. Samples were degassed under dynamic vacuum for 12 hours at 100°C before each measurement. N_2 isotherms were measured using a liquid nitrogen bath (77 K).

Vapor-phase adsorption measurements

For each solid-vapor sorption and fractionation experiment, an open 0.5-ml vial containing 3.0 mg of activated **BrP[5]L** adsorbent (**BrP[5]Lβ**) was placed in a sealed 2-ml vial containing 0.03 ml of solvent or solvent mixture (50:50, v/v). Relative uptake amount in the amorphous solids of **BrP[5]L** was determined by ^{1}H NMR integrals of corresponding proton signals by completely dissolving the organic powders in $CDCl_3$. GC characterizations were also performed to determine the relative uptake amounts of 1-/2-bromoalkane isomers more accurately. Desorption experiments after saturation were carried out by TGA and DSC.

Theoretical calculations

All calculations were performed by DFT using the B3LYP hybrid function combined with 6-31G(d,p) basis set under Gaussian G09. Using single-crystal superstructures as input files, IGM analyses (*47*) were carried out by Multiwfn 3.6 program (*48*) through function 20 (visual study of weak interaction) and visualized using Visual Molecular Dynamics software (*49*).

SUPPLEMENTARY MATERIALS

Supplementary material for this article is available at https://science.org/doi/10.1126/sciadv.abo2255

REFERENCES AND NOTES

1. B. Hua, Y. Ding, L. O. Alimi, B. Moosa, G. Zhang, W. S. Baslyman, J. Sessler, N. M. Khashab, Tuning the porosity of triangular supramolecular adsorbents for superior haloalkane isomer separations. *Chem. Sci.* **12**, 12286–12291 (2021).
2. Y. Zhou, K. Jie, R. Zhao, E. Li, F. Huang, Highly selective removal of trace isomers by nonporous adaptive pillararene crystals for chlorobutane purification. *J. Am. Chem. Soc.* **142**, 6957–6961 (2020).
3. Z. Bao, G. Chang, H. Xing, R. Krishna, Q. Ren, B. Chen, Potential of microporous metal-organic frameworks for separation of hydrocarbon mixtures. *Energ. Environ. Sci.* **9**, 3612–3641 (2016).
4. M. Eddaoudi, J. Kim, N. Rosi, D. Vodak, J. Wachter, M. O'Keeffe, M. Yaghi Omar, Systematic design of pore size and functionality in isoreticular MOFs and their application in methane storage. *Science* **295**, 469–472 (2002).
5. G. Cai, P. Yan, L. Zhang, H.-C. Zhou, H.-L. Jiang, Metal-organic framework-based hierarchically porous materials: Synthesis and applications. *Chem. Rev.* **121**, 12278–12326 (2021).
6. J.-R. Li, J. Sculley, H.-C. Zhou, Metal-organic frameworks for separations. *Chem. Rev.* **112**, 869–932 (2012).
7. M. Yu, R. D. Noble, J. L. Falconer, Zeolite membranes: Microstructure characterization and permeation mechanisms. *Acc. Chem. Res.* **44**, 1196–1206 (2011).
8. L.-H. Chen, M.-H. Sun, Z. Wang, W. Yang, Z. Xie, B.-L. Su, Hierarchically structured zeolites: From design to application. *Chem. Rev.* **120**, 11194–11294 (2020).
9. M. Dusselier, M. E. Davis, Small-pore zeolites: Synthesis and catalysis. *Chem. Rev.* **118**, 5265–5329 (2018).
10. K. Jie, Y. Zhou, Q. Sun, B. Li, R. Zhao, D.-e. Jiang, W. Guo, H. Chen, Z. Yang, F. Huang, S. Dai, Mechanochemical synthesis of pillar[5]quinone derived multi-microporous organic polymers for radioactive organic iodide capture and storage. *Nat. Commun.* **11**, 1086 (2020).
11. J.-S. M. Lee, A. I. Cooper, Advances in conjugated microporous polymers. *Chem. Rev.* **120**, 2171–2214 (2020).
12. D. Wu, F. Xu, B. Sun, R. Fu, H. He, K. Matyjaszewski, Design and preparation of porous polymers. *Chem. Rev.* **112**, 3959–4015 (2012).
13. W. Chen, P. Chen, G. Zhang, G. Xing, Y. Feng, Y.-W. Yang, L. Chen, Macrocycle-derived hierarchical porous organic polymers: Synthesis and applications. *Chem. Soc. Rev.* **50**, 11684–11714 (2021).
14. P. Côté Adrien, I. Benin Annabelle, W. Ockwig Nathan, M. O'Keeffe, J. Matzger Adam, M. Yaghi Omar, Porous, crystalline, covalent organic frameworks. *Science* **310**, 1166–1170 (2005).
15. X. Feng, X. Ding, D. Jiang, Covalent organic frameworks. *Chem. Soc. Rev.* **41**, 6010–6022 (2012).
16. K. Geng, T. He, R. Liu, S. Dalapati, K. T. Tan, Z. Li, S. Tao, Y. Gong, Q. Jiang, D. Jiang, Covalent organic frameworks: Design, synthesis, and functions. *Chem. Rev.* **120**, 8814–8933 (2020).
17. Y. Y. Zhang, J. Y. Duan, D. Ma, P. F. Li, S. W. Li, H. W. Li, J. W. Zhou, X. J. Ma, X. Feng, B. Wang, Three-dimensional anionic cyclodextrin-based covalent organic frameworks. *Angew. Chem. Int. Ed.* **56**, 16313–16317 (2017).
18. X. Li, H.-S. Xu, K. Leng, S. W. Chee, X. Zhao, N. Jain, H. Xu, J. Qiao, Q. Gao, I.-H. Park, S. Y. Quek, U. Mirsaidov, K. P. Loh, Partitioning the interlayer space of covalent organic frameworks by embedding pseudorotaxanes in their backbones. *Nat. Chem.* **12**, 1115–1122 (2020).
19. Y. He, S. Xiang, B. Chen, A microporous hydrogen-bonded organic framework for highly selective C_2H_2/C_2H_4 separation at ambient temperature. *J. Am. Chem. Soc.* **133**, 14570–14573 (2011).
20. I. Hisaki, C. Xin, K. Takahashi, T. Nakamura, Designing hydrogen-bonded organic frameworks (HOFs) with permanent porosity. *Angew. Chem. Int. Ed.* **58**, 11160–11170 (2019).
21. Y. Lin, X. Jiang, S. T. Kim, S. B. Alahakoon, X. Hou, Z. Zhang, C. M. Thompson, R. A. Smaldone, C. Ke, An elastic hydrogen-bonded cross-linked organic framework for effective iodine capture in water. *J. Am. Chem. Soc.* **139**, 7172–7175 (2017).
22. N. Song, T. Kakuta, T.-a. Yamagishi, Y.-W. Yang, T. Ogoshi, Molecular-scale porous materials based on pillar[n]arenes. *Chem* **4**, 2029–2053 (2018).
23. L. L. Tan, H. W. Li, Y. C. Tao, S. X. A. Zhang, B. Wang, Y. W. Yang, Pillar[5]arene-based supramolecular organic frameworks for highly selective CO_2-capture at ambient conditions. *Adv. Mater.* **26**, 7027–7031 (2014).
24. R. S. Patil, A. M. Drachnik, H. Kumari, C. L. Barnes, C. A. Deakyne, J. L. Atwood, Solvent-induced manipulation of supramolecular organic frameworks. *Cryst. Growth Des.* **15**, 2781–2786 (2015).
25. T. Tozawa, J. T. A. Jones, S. I. Swamy, S. Jiang, D. J. Adams, S. Shakespeare, R. Clowes, D. Bradshaw, T. Hasell, S. Y. Chong, C. Tang, S. Thompson, J. Parker, A. Trewin, J. Bacsa, A. M. Z. Slawin, A. Steiner, A. I. Cooper, Porous organic cages. *Nat. Mater.* **8**, 973–978 (2009).

26. T. Mitra, K. E. Jelfs, M. Schmidtmann, A. Ahmed, S. Y. Chong, D. J. Adams, A. I. Cooper, Molecular shape sorting using molecular organic cages. *Nat. Chem.* **5**, 276–281 (2013).
27. A. He, Z. Jiang, Y. Wu, H. Hussain, J. Rawle, M. E. Briggs, M. A. Little, A. G. Livingston, A. I. Cooper, A smart and responsive crystalline porous organic cage membrane with switchable pore apertures for graded molecular sieving. *Nat. Mater.* **21**, 463–470 (2022).
28. L. Atwood Jerry, J. Barbour Leonard, A. Jerga, L. Schottel Brandi, Guest transport in a nonporous organic solid via dynamic van der Waals cooperativity. *Science* **298**, 1000–1002 (2002).
29. P. K. Thallapally, B. Peter McGrail, S. J. Dalgarno, H. T. Schaef, J. Tian, J. L. Atwood, Gas-induced transformation and expansion of a non-porous organic solid. *Nat. Mater.* **7**, 146–150 (2008).
30. K. Jie, Y. Zhou, E. Li, Z. Li, R. Zhao, F. Huang, Reversible iodine capture by nonporous pillar[6]arene crystals. *J. Am. Chem. Soc.* **139**, 15320–15323 (2017).
31. K. Jie, Y. Zhou, E. Li, F. Huang, Nonporous adaptive crystals of pillararenes. *Acc. Chem. Res.* **51**, 2064–2072 (2018).
32. Y. Zhou, K. Jie, R. Zhao, F. Huang, Supramolecular-macrocycle-based crystalline organic materials. *Adv. Mater.* **32**, 1904824 (2020).
33. S. N. Lei, H. Y. Xiao, Y. Zeng, C. H. Tung, L. Z. Wu, H. Cong, BowtieArene: A dual macrocycle exhibiting stimuli-responsive fluorescence. *Angew. Chem. Int. Ed.* **59**, 10059–10065 (2020).
34. D. Luo, J. Tian, J. L. Sessler, X. Chi, Nonporous adaptive calix[4]pyrrole crystals for polar compound separations. *J. Am. Chem. Soc.* **143**, 18849–18853 (2021).
35. J. R. Wu, B. Li, Y. W. Yang, Separation of bromoalkanes isomers by nonporous adaptive crystals of leaning pillar[6]arene. *Angew. Chem. Int. Ed.* **59**, 2251–2255 (2020).
36. J.-R. Wu, Y.-W. Yang, Geminiarene: Molecular scale dual selectivity for chlorobenzene and chlorocyclohexane fractionation. *J. Am. Chem. Soc.* **141**, 12280–12287 (2019).
37. T. Ogoshi, T.-a. Yamagishi, Y. Nakamoto, Pillar-shaped macrocyclic hosts pillar[n]arenes: New key players for supramolecular chemistry. *Chem. Rev.* **116**, 7937–8002 (2016).
38. D. Xia, P. Wang, X. Ji, N. M. Khashab, J. L. Sessler, F. Huang, Functional supramolecular polymeric networks: The marriage of covalent polymers and macrocycle-based host-guest interactions. *Chem. Rev.* **120**, 6070–6123 (2020).
39. Z. Li, Y.-W. Yang, Functional materials with pillarene struts. *Acc. Mater. Res.* **2**, 292–305 (2021).
40. J.-R. Wu, Z. Cai, G. Wu, D. Dai, Y.-Q. Liu, Y.-W. Yang, Bottom-up solid-state molecular assembly via guest-induced intermolecular interactions. *J. Am. Chem. Soc.* **143**, 20395–20402 (2021).
41. Y. Zhou, K. Jie, R. Zhao, E. Li, F. Huang, Cyclic ether contaminant removal from water using nonporous adaptive pillararene crystals via host-guest complexation at the solid-solution interface. *Research* **2019**, 5406365 (2019).
42. G. M. Sheldrick, Experimental phasing with SHELXC/D/E: Combining chain tracing with density modification. *Acta Crystallogr. D Biol. Crystallogr.* **66**, 479–485 (2010).
43. G. M. Sheldrick, SHELXT - Integrated space-group and crystal-structure determination. *Acta Crystallogr. A Found. Adv.* **71**, 3–8 (2015).
44. G. M. Sheldrick, A short history of SHELX. *Acta Crystallogr.* **64**, 112–122 (2008).
45. G. M. Sheldrick, Crystal structure refinement with SHELXL. *Acta Crystallogr. C Struct. Chem.* **71**, 3–8 (2015).
46. O. V. Dolomanov, L. J. Bourhis, R. J. Gildea, J. A. K. Howard, H. Puschmann, Olex2: A complete structure solution, refinement and analysis program. *J. Appl. Cryst.* **42**, 339–341 (2009).
47. C. Lefebvre, G. Rubez, H. Khartabil, J. C. Boisson, J. Contreras-Garcia, E. Henon, Accurately extracting the signature of intermolecular interactions present in the NCI plot of the reduced density gradient versus electron density. *Phys. Chem. Chem. Phys.* **19**, 17928–17936 (2017).
48. T. Lu, F. W. Chen, Multiwfn: A multifunctional wavefunction analyzer. *J. Comput. Chem.* **33**, 580–592 (2012).
49. W. Humphrey, A. Dalke, K. Schulten, VMD: Visual Molecular Dynamics. *J. Mol. Graph.* **14**, 33–38 (1996).
50. J.-R. Wu, A. U. Mu, B. Li, C.-Y. Wang, L. Fang, Y.-W. Yang, Desymmetrized leaning pillar[6] arene. *Angew. Chem. Int. Ed.* **57**, 9853–9858 (2018).

Acknowledgments

Funding: This work was supported by the National Natural Science Foundation of China (grant nos. 52173200 and 21871108), the China Postdoctoral Science Foundation (grant no. BX2021112), and Jilin Province-University Cooperative Construction Project–Special Funds for New Materials (grant no. SXGJSF2017-3). **Author contributions:** Conceptualization: J.-R.W. and Y.-W.Y. Methodology: J.-R.W. and G.W. Investigation: J.-R.W. and G.W. Visualization: J.-R.W. and Y.-W.Y. Supervision: Y.-W.Y. Writing (original draft): J.-R.W., G.W., D.L., and D.D. Writing (review and editing): Y.-W.Y. **Competing interests:** The authors declare that they have no competing interests. **Data and materials availability:** All data needed to evaluate the conclusions in the paper are present in the paper and/or the Supplementary Materials. X-ray crystallographic data reported here are listed in the Supplementary Materials and archived at the Cambridge Crystallographic Data Centre under reference numbers CCDC 2041500, 2041451, 2041449, 2041446, 2041448, 2041450, 2124278, 2124280, 2124276, 2124288, and 2124291.

Submitted 21 January 2022
Accepted 18 April 2022
Published 3 June 2022
10.1126/sciadv.abo2255